ACS APPLIED MATERIALS & INTERFACES

www.acsami.org

Research Article

Molecular Engineered Carbon-Based Sensor for Ultrafast and Specific Detection of Neurotransmitters

Jagadeesh Suriyaprakash, Kanchan Bala, Lianwei Shan, Lijun Wu,* and Neeraj Gupta*

Cite This: *ACS Appl. Mater. Interfaces* 2021, 13, 60878−60893

Read Online

ACCESS | Metrics & More | Article Recommendations | Supporting Information

ABSTRACT: In the quest for designing affordable diagnostic devices with high performance, precisely functionalized carbon-based materials with high accuracy and selectivity are required. Every material has its own unique ability to interact with the analyte, and its performance can be enhanced by probing the interaction mechanism. Herein, *p*-aminophenol (PAP)-functionalized reduced graphene oxide (rGO) nanoscale material is developed by a one-step synthetic route as an all-organic-based sensor. As the PAP molecules are precisely covalently interacted with the rGO at the basal plane and form a wrinkled-paper-like structure, the functionalized material exhibits an outstanding sensing ability (7.5 nM neurotransmitter dopamine (DA) at a wide linear range, 0.01−100 μM) with fast electrical transduction (<3 s) and good recyclability (~10 cycles) in a real sample. Combining various analytical and density functional theory (DFT) calculation methods, physicochemical properties and the interaction mechanism of analyte−materials transduction are discussed exclusively. Besides, the potential application of the well-dispersed rGO-PAP gravure ink in flexible-printed electronics fields is explored. This study not only provides new insights into the surface/interface chemistry and working principle of this unique anchoring of PAP on rGO but also offers a new pathway for developing other forms of metal-free/organic functionalized biosensors with high efficiency.

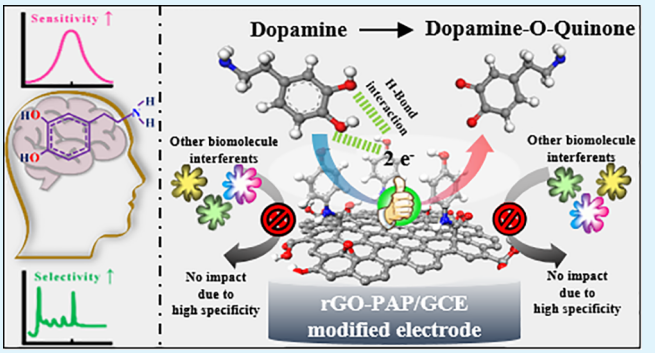

KEYWORDS: *2D materials, electrocatalysis, bioelectronics, neurotransmitter, functionalization, dopamine, biosensor*

1. INTRODUCTION

Accurate diagnosis of neurological diseases to provide affordable health services to the user end is always required in the current health care system. Critical neurological diseases are mostly associated with the dysfunction of dopamine (DA) neurotransmitter in our nervous system.[1] This is found in human blood and serum in extremely tiny amounts [10^{-9}−10^{-5} mol L^{-1} (hereafter M)] along with other biomolecules.[2] Therefore, the advancement of noninvasive probing systems for the detection of DA is highly desirable. Such sensing probes must provide excellent specificity and sensitivity (tens of nM to hundreds of pM) while being inexpensive for commercial use. Over the last three decades, extensive sensing techniques have been employed for the detection of neurotransmitters.[3−13] Among them, the electrochemical sensing technique(s) excel in point-of-care (POC) tests, fast readout, accuracy, and real-time monitoring.[11,12] This technique further relies on the efficiency of the probing materials often designed with the help of metal-based,[14−18] metal-free,[19−21] and their hybrid[22−27] materials.

Since metal-free/organic-based sensors outperform metal-based/hybrid sensors in terms of their nontoxicity, sustainability, affordability, reproducibility, and flexibility in comparison to metal-based sensors, they are widely utilized in electrochemical biosensing techniques.[28,29] However, these sensors have limitations associated with their electronic nature, chemical stability, and fouling behavior. If the attached organic molecule does not have conjugated electrons in its structures, it is hard to control the electron movement in the resulting material. Also, the chemically tagged organic molecules are prone to hydrolysis during operational conditions. The different functional groups present on the surface of organic molecules can combine with different biomolecules and show a rapid fouling behavior, making their reproducibility challenging. Hence, finding a suitable organic molecule for tagging onto the surface of appropriate support is a challenging task, which makes exploration of this research field wide open to date. For instance, a carbon-based sensor was developed by combining the conjugated organic molecule polyaniline

Received: September 20, 2021
Accepted: December 7, 2021
Published: December 17, 2021

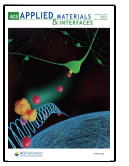

https://doi.org/10.1021/acsami.1c18137
ACS Appl. Mater. Interfaces 2021, 13, 60878−60893

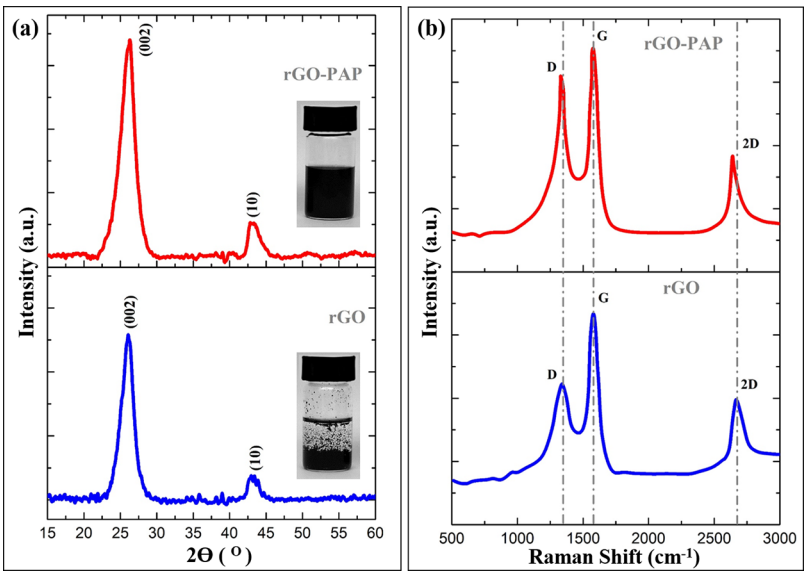

Figure 1. (a/b) XRD/Raman spectra of the pristine rGO and PAP-functionalized rGO; the insets are the photographic images of the respective materials dispersed in H_2O.

(PANI) with graphene support[30] that was later combined with an aptamer. The aptamer-based organic sensor showed an excellent detection limit to a very low pM level of DA, failed in its stability, and did not provide a solution to fabricate an affordable device. A recent study of an electrochemically reduced rGO-based sensor proved that it has very good stability and specificity toward the detection of DA but failed in providing sensitivity and durability.[31] A very recent study by Butler et al. demonstrated that a modified commercial graphene ink possessed excellent sensitivity (5 pM) and selectivity toward DA, but its durability, affordability, and antifouling properties are questionable.[32] All of these studies show that GO alone has a limited potential to develop a good sensor for DA detection, and there is a great scope to increase its sensitivity and selectivity by modifying its surface.

To this end, various carbon/organic-based materials have been developed by exploiting their π electron mobility,[32] point defects,[33] basal/edge plane chemistry,[34,35] and oxygen-containing functional groups.[36] Various parameters required to design an efficient material for biosensing application are tabulated in Table S1. After considering these factors, it can be concluded that the incorporation of heteroatoms such as nitrogen can enhance the electrocatalytic activity and conductivity. Moreover, the increase in $\pi-\pi$ conjugation by incorporating some electron-rich molecules or conducting polymers can significantly enhance the sensitivity, selectivity, and conductivity. However, these approaches lack a qualitative and quantitative understanding of the precise relationship between the analyte and material, followed by electrical transductions.

Herein, we come up with a new strategy to design an all-organic-based high-performance electrochemical biosensor for DA detection by grafting an electron cloud-rich simple organic molecule *p*-aminophenol (PAP) on the basal plane of two-dimensional (2D) carbon material (rGO) via covalent linkage. rGO-based materials have various active sites (defects and −OH/−COOH functional groups) and tunable physicochemical characteristics[37,38] in comparison to other 2D carbon materials that can be utilized to design an efficient selective and sensing material for the detection of DA[39−45] through the optimization of electronic and surface features. The outstanding sensing behavior of the developed biosensor is found to originate from the rapid charge transfer occurring via $\pi-\pi$ electron coupling of rGO-PAP linkage and a special type of hydrogen bond formed between rGO-PAP and DA. To the best of our knowledge, this rationally designed all-organic-based single-component biosensor is the first example of a DA neurotransmitter measuring extremely low quantities up to the nM level with fast readout.

2. RESULTS AND DISCUSSION

2.1. Structural and Morphological Evaluation of rGO-PAP. The measured X-ray diffraction patterns (XRD) of the pristine rGO and as-synthesized rGO-PAP samples exhibit a well-crystalline graphitic nature as displayed in Figure 1a. The spectra were recorded in a range of $2\theta = 10-60°$; peaks at 25.6 and 43.2° are attributed to (002) and two-dimensional (10) planes, respectively. There is typical peak broadening and increasing in the intensity of the rGO-PAP sample with respect to the pristine sample, which argues a significant increase in spacing due to the intercalation of PAP functional groups in the interlayers of rGO. To decipher the crystallographic information of the synthesized rGO-PAP functional material, Bragg and Scherrer equations were used to calculate the interlayer distances of the graphene sheets as well as the average diameter and height of the stacking layers. The results show that the rGO-PAP consists of four to five layers in stacking nanostructures each distanced at 0.52 nm. Table S2 compares the structural parameters of rGO-PAP and pristine rGO. The insets in Figure 1a correspond to the water-dispersed samples. Unlike pristine rGO, rGO-PAP is uniformly dispersed in water owing to the surface modification by the PAP molecules without any residue at the bottom.

Raman spectroscopy can be utilized to examine the strain, defects, and disorders induced by the functionalization of the graphene nanostructures. Figure 1b depicts the typical Raman spectra of rGO and rGO-PAP with D, G, and 2D peaks. The D band represents the structural disorder of sp^2 domains and C−C sp^2 bond stretching, whereas the G band stands for the degree of graphitization. The peak of 2D is the second order of

https://doi.org/10.1021/acsami.1c18137
ACS Appl. Mater. Interfaces 2021, 13, 60878−60893

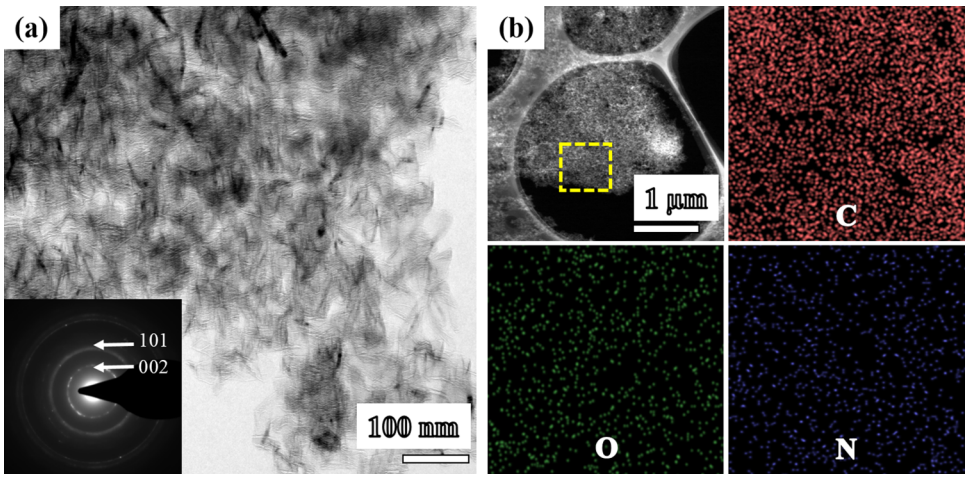

Figure 2. (a) TEM image of rGO-PAP; the inset is the corresponding selected area electron diffraction (SAED) image. (b) Energy-dispersive spectroscopy (EDS) mapping images of rGO-PAP. The bright black and white image corresponds to the high-angle annular dark-field-scanning transmission electron microscopy (HAADF-STEM), and the scanning region indicated by the yellow rectangle marks the element analysis area.

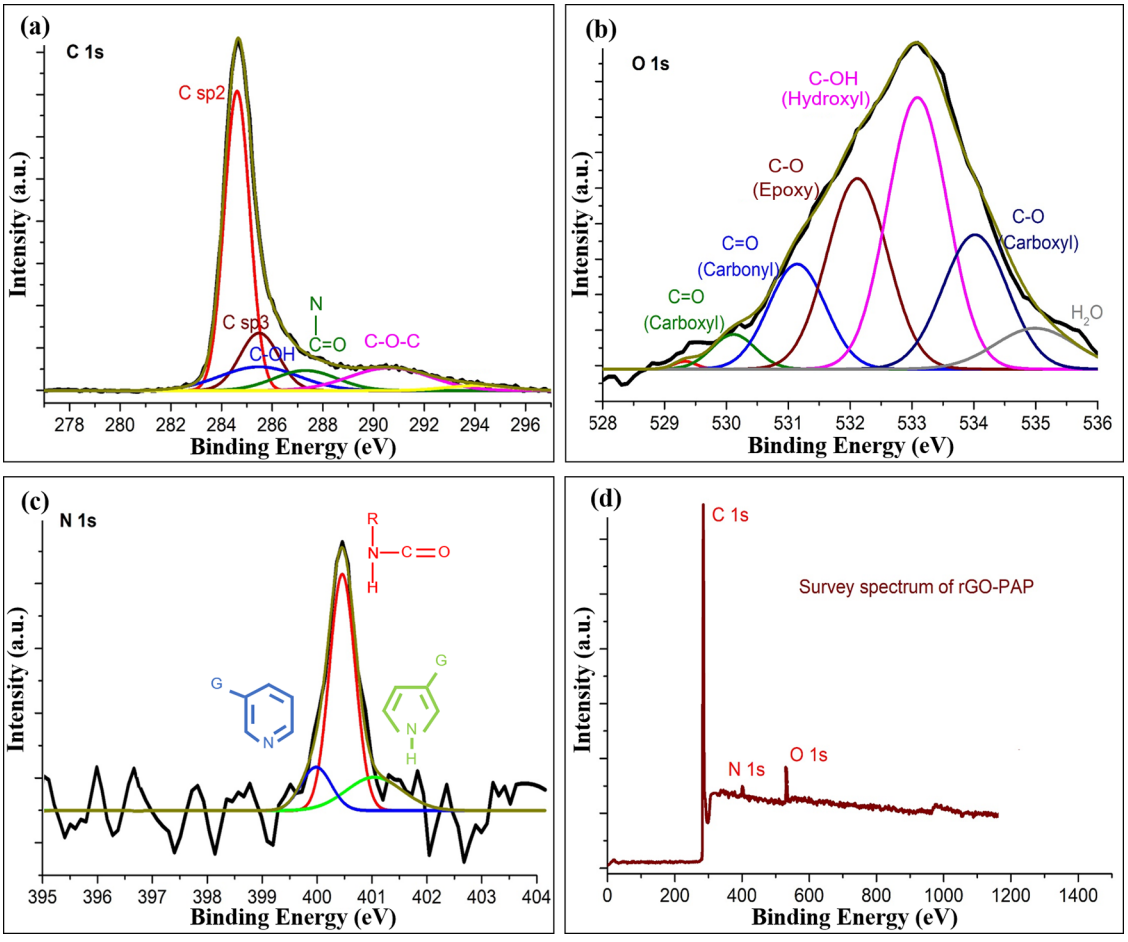

Figure 3. XPS spectra of rGO-PAP. (a) Carbon, (b) oxygen, and (c) nitrogen core-level spectra. All spectra are plotted with deconvoluted spectra. The corresponding chemical species are denoted near the peaks. (d) Survey spectrum.

the D peak and can be used as a reference to determine the electron−hole doping in graphene-based materials.

The as-synthesized rGO-PAP reveals three characteristic bands at D (1344 cm^{-1}), G (1573 cm^{-1}), and 2D (2684 cm^{-1}). The intensity ratio I_D/I_G increases after rGO is functionalized by PAP probably due to the attachment of PAP molecules to the basal plane of the rGO and the separation of the layered structure.[46] Generally, the peak position of 2D remains nearly unaffected by electron doping concentrations up to ~1.5 × 10^{13} cm^{-2}. It shifts down or up[47,48] upon electron or hole doping, respectively. An obvious downshift (10 cm^{-1}) of the 2D peak position can be observed when rGO is attached to PAP as shown in Figure 1b. This can be attributed to the electron doping through the interaction

https://doi.org/10.1021/acsami.1c18137
ACS Appl. Mater. Interfaces 2021, 13, 60878−60893

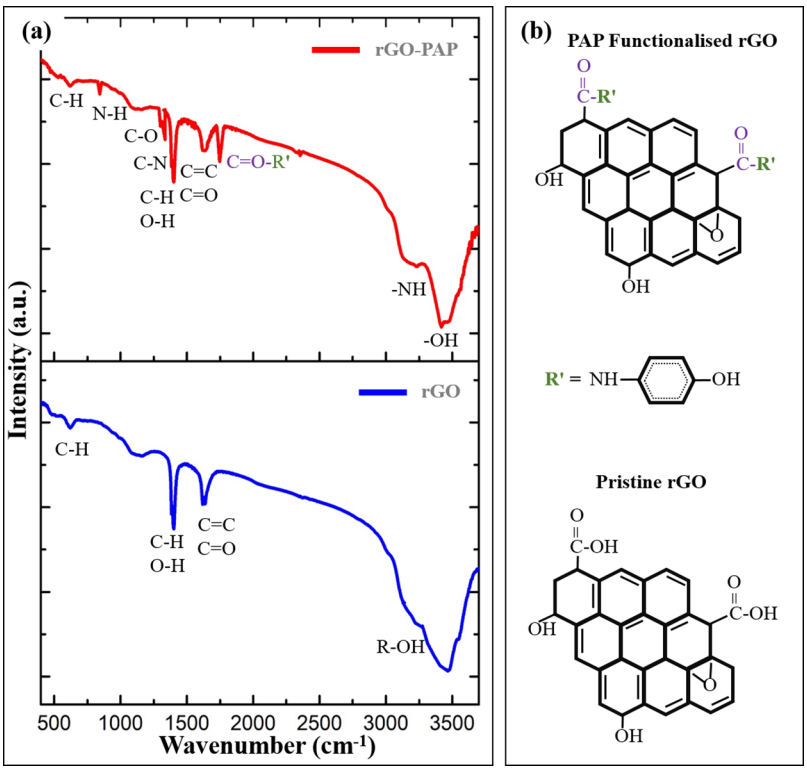

Figure 4. (a) FT-IR spectra of the pristine rGO and as-synthesized rGO-PAP display various peaks attributed to C−H, C═C, C═O, C−O−C, −N−C═O, and −OH functional groups. (b) Schematic illustration of the functional group and bonding nature of the pristine rGO and as-synthesized rGO-PAP.

between PAP and rGO, indicating that the surface of the rGO has been fruitfully altered by the PAP molecules.

The transmission electron microscopy (TEM) image in Figure 2a illustrates that the rGO-PAP nanostructure shows a wrinkled-paper-like morphology. This wrinkled configuration governs the surface feature of the rGO sheet and is most probably caused by the reaction between rGO and PAP during the synthetic process. The selected area electron diffraction (SAED) pattern in the inset of Figure 2a exhibits a typical sharp polycrystalline ring pattern consisting of many diffraction spots, indicating the loss of the long-range order between the rGO 2D nanostructures. The bright spots can be well indexed to the (002) and (10) planes of the short-range ordered rGO, which is consistent with the measured XRD result. Figure 2b illustrates high-angle annular dark-field (HAADF)−energy-dispersive spectroscopy (EDS) elemental mapping images of the rGO-PAP. The yellow rectangle represents a scanned region. As expected, the most abundant element carbon (C) is uniformly distributed throughout the sample, whereas the oxygen (O) and nitrogen (N) are randomly distributed in the matrix. The amounts of these three elements are summarized in Table S4. This confirms that the synthesized rGO-PAP material has a nitrogen group-functionalized rGO surface, owing to the chemical interaction between PAP and rGO nanosheets.

2.2. Surface and Bonding Nature of rGO-PAP. The elemental composition of the as-synthesized rGO-PAP is examined by X-ray photoelectron spectroscopy (XPS) and Gaussian fitting. Three peaks corresponding to C 1s (284.6 eV), N 1s (400 eV), and O 1s (531.8 eV) species can be observed in the XPS survey spectrum of the sample (Figure 3d). The traceable amount of nitrogen indicates that the PAP molecules are attached to the rGO matrix, which is consistent with the EDS results.

The high-resolution core-level spectra shown in Figure 3a−c reveal the content of the carboxyl, hydroxyl, carbonyl, amine moieties, pyridinic N, and pyrrolic N in the as-synthesized rGO-PAP. The C 1s spectrum can be deconvoluted into one major component and four minor components (Figure 3a). The major peak at 284.6 eV is attributed to C sp^2, whereas the four minor peaks at 285.6, 285.8, 287.4, and 290.7 eV correspond to the functional groups C sp^3, C−OH, C═O/C−O−C, and −COOH. Especially, the peak at 287.4 eV indicates that carbon is linked to the amide bond (−N−C═O). Similarly, the O 1s spectrum can be deconvoluted into five components in the range of 530−534 eV.[49−51] The major peak at a higher binding energy 533.1 eV is assigned to C−O epoxy, while the second major component at a lower binding energy 532.1 eV is assigned to hydroxyl oxygen in the rGO-PAP. After functionalization, an increase in the intensity of the C sp^2 peak is observed, while the decrease of the C−O peak intensity authorizes that various oxygen-containing groups have been successfully involved in the addition of the nitrogen groups.

As shown in Figure 3c, the N 1s spectrum can be deconvoluted into one major and two minor components in the range of 399.8−401.3 eV. The peak at 400.6 eV can be attributed to the amide bond linked between amine moieties of PAP molecule and −COOH of rGO.[52] The lower-binding-energy component at 399.8 eV is assigned to the pyridinic nitrogen and the higher energy at 401.3 eV is to the pyrrolic nitrogen in the modified rGO structure. The two minor peaks in the spectrum depict that the as-synthesized rGO-PAP sample consists of amide-type functional groups rather than excess nitrogen-doped graphene structures usually formed by

https://doi.org/10.1021/acsami.1c18137
ACS Appl. Mater. Interfaces 2021, 13, 60878−60893

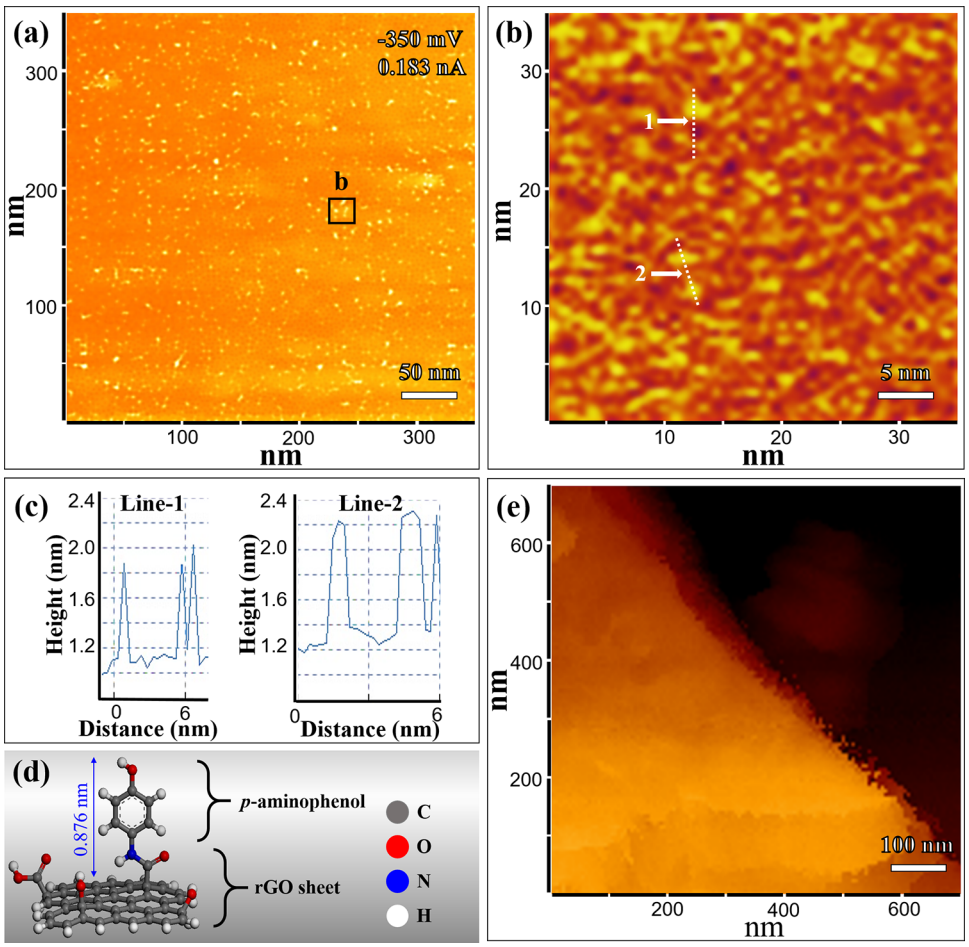

Figure 5. (a) STM image of rGO-PAP. (b) High-resolution STM image of the area squared in (a). (c) Line profiles; Line-1 and Line-2 are indicated as white dotted lines in (b). (d) Simulated structure of rGO-PAP. (e) Topographic AFM image of rGO-PAP.

aminophenol functionalization at the higher annealing temperature. These results evidence the existence of C−N−C═O-type covalent linkage formed during the synthetic process.

The bonding nature and surface functional groups of the as-prepared rGO-PAP are also explored by Fourier transform infrared (FT-IR) analysis. As shown in Figure 4, the peaks of the C−H, C═C, C═O, C−O−C, and OH functional groups can be clearly observed both in the pristine rGO and the as-prepared rGO-PAP. Comparing the region of 700−1750 cm^{-1} in the two spectra, significant changes can be found in rGO-PAP due to the formation of new structures. It implies that there is an interaction between PAP and the carbonyl group of the rGO during the functionalization process. Moreover, new peaks at 850, 1320, 1340, 1740, and 3400 cm^{-1} corresponding to the N−H, COO, C−N, and R−OH groups can be observed in the FT-IR spectrum of the rGO-PAP along with the pristine rGO characteristic peaks. This argues that there are hydroxyl, carbonyl, and amide groups in rGO-PAP, which is consistent with the XPS results.

It is known that the surface modification of the graphene oxide by aminophenol molecule tends to form covalent linkage via carboxyl, amino, and a hydroxyl group, resulting in either amide- or ester-type bonds in the molecules. The FT-IR study has confirmed the presence of the amide features; therefore, we believe that the covalent linkage occurred between the carboxyl sites of rGO and amine sites of PAP, which exhibits aromatic amide-type bonding nature with hydroxyl group terminals to some extent in the functionalized rGO. The solid-state $^{13}C/^{1}H$ NMR analysis is carried out to provide further insight into the molecular arrangement in as-synthesized rGO-PAP (Figure S1). The finding, as expected, indicates the presence of an amide bond between rGO and PAP, which is established by the −COOH site of rGO and the $-NH_2$ site of PAP.

Scanning tunneling microscopy (STM) and atomic force microscopy (AFM) techniques are utilized to visualize and estimate the surface coverage of the covalent attachment sites between the PAP molecule and rGO at the nanoscale level. Figure 5a shows the STM image of rGO-PAP observed on the basal plane site. The uniformly distributed bright spots on the basal plane sites represent the anchoring sites of the PAP molecules. A high-resolution scanned area is displayed in Figure 5b. It can be seen that the low- and high-intensity bright spots are distributed on the surface. These might be due to the presence of various charges belonging to different functional groups such as −OH, −COO, and PAP.

Although the image is blurred by the natural roughness of the bottom layer, it displays a clear wrinkled-paper-like morphology and surface coverage of the rGO-PAP. The height profile and width of the spots are measured to be 0.8−1 nm and 0.5 ± 0.1 nm as shown in Figure 5c. The simulated molecular anchoring height was calculated to be 0.876 nm (Figure 5d) and is in agreement with the experimental value. This result is also consistent with the earlier works describing an electrochemical grafting technique on a graphite/graphene

https://doi.org/10.1021/acsami.1c18137
ACS Appl. Mater. Interfaces 2021, 13, 60878−60893

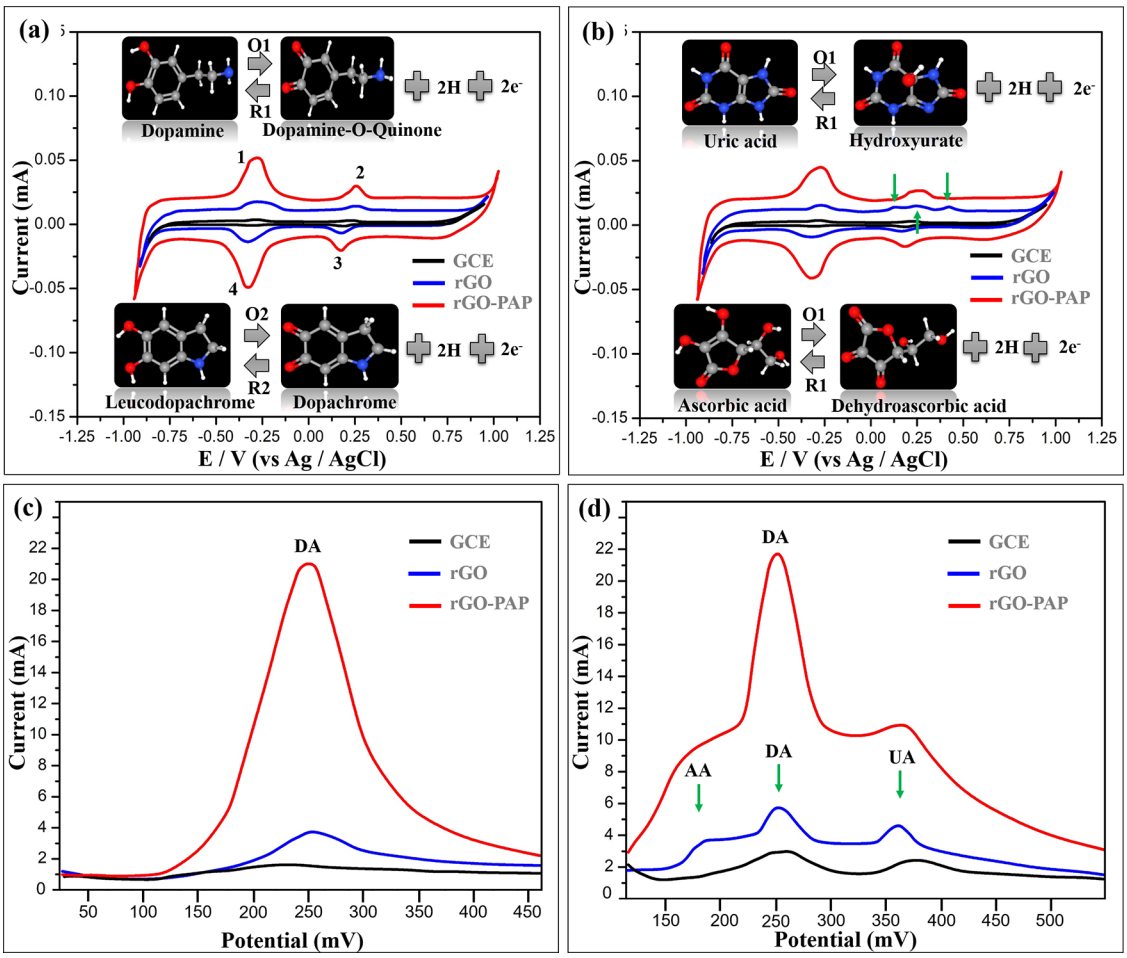

Figure 6. (a/b) Cyclic voltammograms of the bare, pristine rGO, and rGO-PAP-modified electrodes in the blank phosphate buffer solution (PBS) with pH = 7.20 containing 0.05 mM DA solution/0.05 mM DA + 0.5 mM uric acid + 1 mM ascorbic acid at a scan rate of 100 mV s^{-1}. Insets demonstrate the electrochemical reaction mechanisms. (c/d) DPVs of the bare, pristine rGO, and rGO-PAP-modified electrodes in the blank PBS with pH = 7.20 containing 0.05 mM DA solution/in the presence of the mixture containing 0.05 mM DA, 0.5 mM uric acid, and 1 mM ascorbic acid.

surface.[53,54] However, our grafting method is more efficient because the cluster formation is avoided due to the anchoring of multiple molecules and controlled functionalization on the host surface. A typical topographic AFM image in Figure 5e displays a layered structure taken near the edges of rGO-PAP.

2.3. Electrochemical Characteristics of the rGO-PAP Electrode. The electrochemical activities of the modified and bare electrodes toward the oxidation of DA are explored by the cyclic voltammetry (CV) and differential pulse voltammetry (DPV) studies at various concentrations with potential interference. Figure 6a depicts the cyclic voltammograms of the bare glassy carbon electrode (GCE), pristine rGO, and rGO-PAP-modified electrodes in the presence of 0.05 mM DA. For bare GCE and pristine rGO, no significant redox peaks appear. On the other hand, significant redox peaks are observed for the rGO-PAP-modified electrode. Two oxidation peaks and two reduction peaks with different peak currents and potentials can be observed in the CV curves. The rGO-PAP-modified electrode displays an anodic peak (E_{pa}) at 0.25 V and a cathodic peak (E_{pc}) at 0.09 V with the current response of 22 μA (ΔE_p = 0.16 V). The four distinct peaks observed in the CV curve refer to the following reactions

$$\text{leucodopachrome} \rightarrow \text{dopachrome} + 2H^+ + 2e^- \quad (1)$$

$$\text{dopamine} \rightarrow \text{dopamine} - O - \text{quinone} + 2H^+ + 2e^- \quad (2)$$

$$\text{dopamine} - O - \text{quinone} + 2H^+ + 2e^- \rightarrow \text{dopamine} \quad (3)$$

$$\text{dopachrome} + 2H^+ + 2e^- \rightarrow \text{leucodopachrome} \quad (4)$$

Thus, the reactions of the DA neurotransmitter are associated with the second peak of oxidation and the first peak of reduction. In the forward CV scan (−1.0 to 1.0 V, refer to Figure 6a,b), DA is adsorbed onto the working electrode, while electrons and dopamine-*O*-quinone are released outward from the working electrode. In the reverse scan (+1.0 to −1.0 V), dopamine-*O*-quinone is reduced to dopamine as illustrated in Figure 6a (inset).

The selectivity and cross-reactivity of the rGO-PAP modified electrode for DA sensing are also explored in the presence of the two common potential interfering agents, uric acid (UA) and ascorbic acid (AA).[55] It is well known that the oxidation peak potentials for AA, UA, and DA are very close to each other and it is challenging to distinguish these molecules. We compared the performance of the bare, pristine rGO, and rGO-PAP-modified electrodes in a mixture containing 0.05 mM DA, 0.5 mM UA, and 1 mM AA. As shown in Figure 6b,

https://doi.org/10.1021/acsami.1c18137
ACS Appl. Mater. Interfaces 2021, 13, 60878−60893

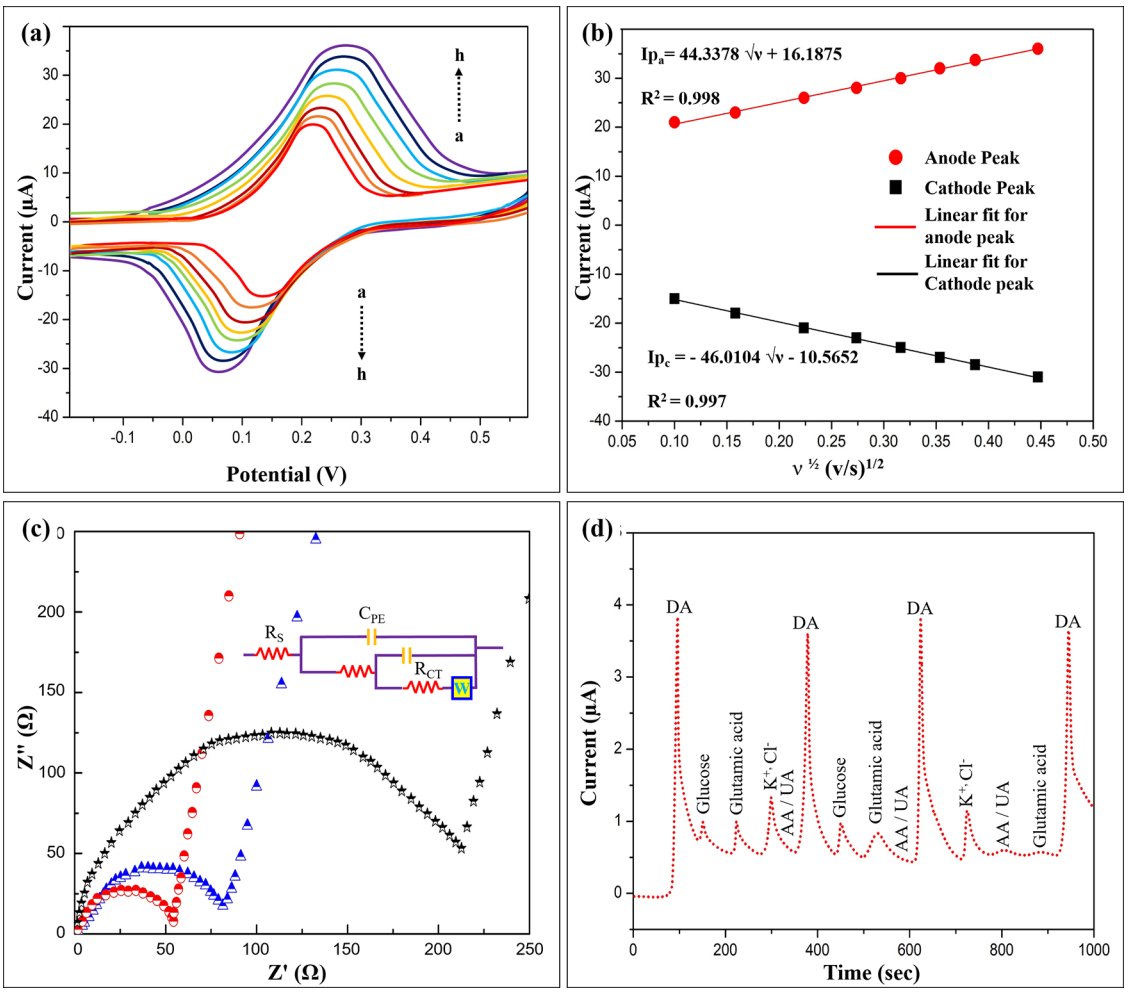

Figure 7. (a) CV of the rGO-PAP electrode at various scan rates (a–h: 0.01, 0.025, 0.05, 0.075, 0.1, 0.125, 0.15, and 0.2 mV s^{-1}, respectively) in 0.05 mM DA. (b) I_{pa} and I_{pc} versus $\sqrt{\nu}$. (c) EIS of bare GCE (black), pristine rGO (blue), and rGO-PAP (red) with 2 mM $K_3[Fe(CN)_6]$/$K_4[Fe(CN)_6]$ in 0.1 M KCl solution. (d) Amperometry specificity study of the rGO-PAP and electrocatalytic oxidation of DA (10 μM) along with equimolar AA, UA, KCl, glucose, and glutamic acid, operated at a potential of +0.25 V in PBS.

the catalytic current of DA oxidation at the rGO-PAP electrode attains a maximum value at a potential of 0.25 V with a current response of 21.4 μA. The peak corresponding to DA is single and distinct on the rGO-PAP electrode, whereas those on the pristine rGO and bare GCE exhibit three and two broad anodic peaks, respectively. It is worth noting that the amounts of AA and UA are 10-fold and 20-fold of DA, respectively, in the whole paper when investigating the selectivity. These outcomes prove that rGO-PAP has excellent selectivity and sensitivity for detecting DA. The three distinct peaks observed in the CV for the pristine rGO at 0.13, 0.25, and 0.36 V are assigned to the oxidation potential of AA, DA, and UA, respectively, which refer to the following oxidation reactions

$$\text{ascorbic acid} \rightarrow \text{dehydroascorbic acid} + 2H^+ + 2e^- \quad (5)$$

$$\text{dopamine} \rightarrow \text{dopamine} - O - \text{quinone} + 2H^+ + 2e^- \quad (6)$$

$$\text{uric acid} \rightarrow \text{hydroxyurate} + 2H^+ + 2e^- \quad (7)$$

To further study the exact sensitivity and analytical capability of the rGO-PAP against DA, the DPV method is used with/without the interference of other molecules. All of the anode current response was obtained at about 0.25 V with 0.05 mM DA. As shown in Figure 6c, an obvious peak due to DA oxidation on the rGO-PAP electrode can be observed, whereas no significant signal was observed on the bare GCE and pristine rGO electrodes. Figure 6d exhibits a very strong and distinct DA peak along with two minor shoulder peaks in the rGO-PAP electrode. It is observed that the variation of the current response is less than 1% in the presence of 20 times higher concentration of potential interferents than the DA alone. For the bare GCE and pristine rGO electrodes, only two and three broad peaks can be observed. The signal of DA and the two interferents overlap with each other, leading to poor selectivity. Moreover, the low current response means poor sensitivity. These findings prove that the rGO-PAP electrochemical sensor demonstrates excellent selectivity for the detection of DA with a selectivity coefficient of ≈1.

2.3.1. Electrocatalytic Behavior Analysis. To decipher the exact mechanism of the electrocatalytic oxidation of DA at the rGO-PAP electrode, the influence of the scan rate and the electrochemical impedance spectroscopy (EIS) studies were investigated. Figure 7a shows the influence of the scan rate (ν) during the CV study at scan rates of 0.01, 0.025, 0.05, 0.075, 0.1, 0.125, 0.15, and 0.2 mV s^{-1} in 0.05 mM DA. The current (I) response increases with the scan rate, and the redox peak potential (anodic peak, E_{pa} and cathodic, E_{pc}) displays a

https://doi.org/10.1021/acsami.1c18137
ACS Appl. Mater. Interfaces 2021, 13, 60878–60893

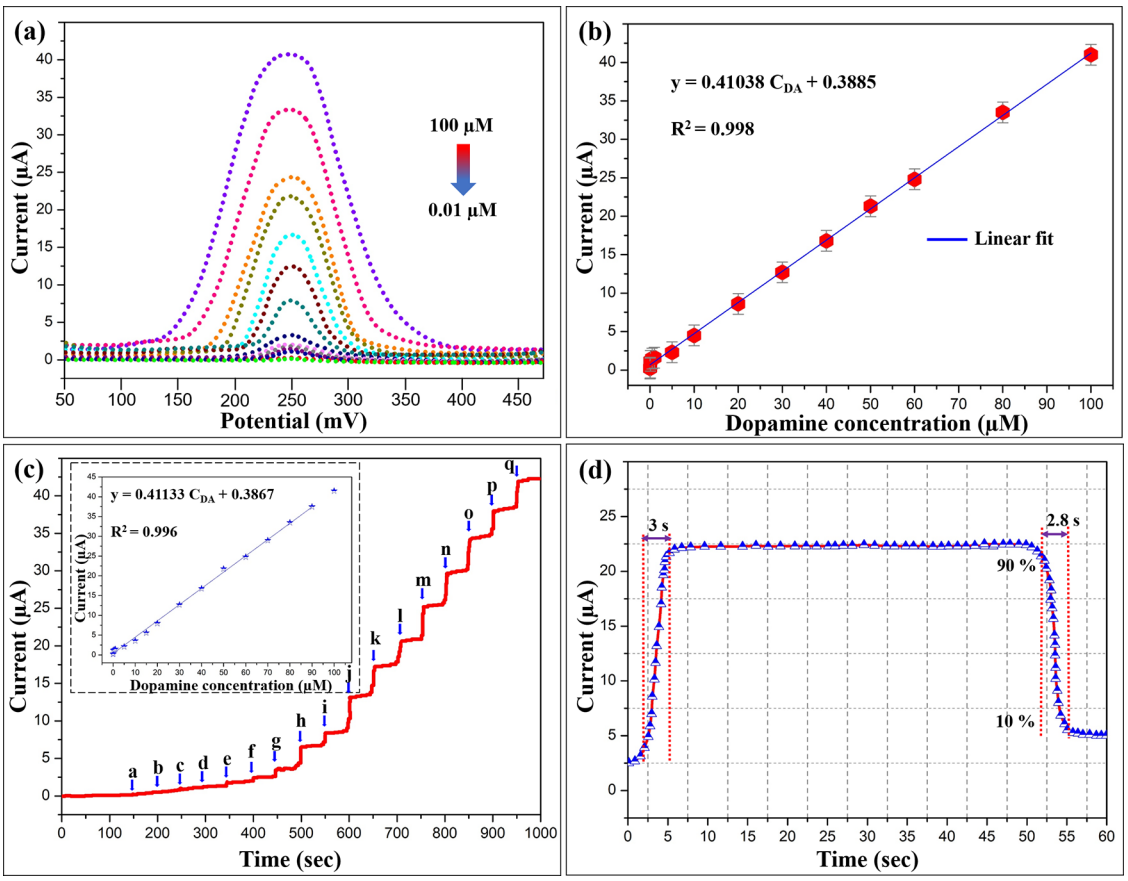

Figure 8. (a) DPV curves of the rGO-PAP-modified electrode for various concentrations of dopamine (0.01−100 μM) along with 20 μM AA and UA in the 100 mM PBS solution. (b) Calibration curve of current versus DA concentration. Error bar: standard deviation of eight samples measurement (n = 8). (c) Amperometry curve of the rGO-PAP-modified electrode for successive addition of various concentrations of DA (a−q: 0.01−100 μM, respectively) at a potential of +0.25 V in the PBS solution (injections carried out at regular intervals of 50 s). The inset is the calibration curve of the current versus DA concentration. (d) Response recovery curve for 50 μM DA.

positive shift. As shown in Figure 7b, the relationship between the current response and the square root of the scan rate shows good linearity: I_{pa} = 44.3378 $\sqrt{\nu}$1 + 16.1875 and I_{pc} = −46.0104 $\sqrt{\nu}$ − 10.5652. This argues that the electrocatalytic reaction of DA on the rGO-PAP is a diffusion-controlled process.[56] The linear relationship of E_{pa} and E_{pc} plotted against ln ν is shown in Figure S2. It is well known that the charge transfer coefficient (α), electron transfer number (n), and heterogeneous rate constant (K_s) can be calculated using the following Laviron equations.[57]

$$E_{pa} = E^0 + \frac{RT}{(1-\alpha)nF} \ln \nu \quad (8)$$

$$E_{pc} = E^0 - \frac{RT}{\alpha nF} \ln \nu \quad (9)$$

$$\log K_s = \alpha \log(1-\alpha) + (1-\alpha)\log \alpha - \log \frac{RT}{nF\nu} - \frac{(1-\alpha)\alpha nF\Delta E_p}{2.3\,RT} \quad (10)$$

where F and R are the Faraday and molar gas constants, respectively, and T is the temperature. By combining eqs 8 and 9 and the slope values obtained from Figure S2, α and n are calculated to be 0.8 and 1.7, respectively. Substituting these values into eq 10, the value of K_s is calculated to be 1.28 s^{-1}. This is larger than the earlier reported values of other carbon-based electrodes,[58,59] indicating fast electron transfer kinetics during the interaction between DA and rGO-PAP.

The interface properties of the modified electrodes are investigated by the electron impedance spectroscopy (EIS) study (operated from 10^{-1} to 10^5 Hz at an amplitude of 5 mV). As illustrated in Figure 7c, the semicircle portion of the Nyquist plot can be attributed to the charge transfer resistance (R_{CT}) caused by the electron transfer of the redox probe $[Fe(CN)]^{3-/4-}$. The R_{CT} value is estimated to be 205, 85, and 55 Ω for bare GCE, pristine rGO, and rGO-PAP, respectively. The lower R_{CT} value of rGO-PAP discloses that the electron transfer resistances are significantly reduced by PAP anchoring due to a large number of π-electron sites in rGO-PAP.

To understand the specificity of the rGO-PAP electrode for electrocatalytically oxidizing DA, an amperometry technique is employed in the presence of AA, UA, KCl, glucose, and glutamic acid at a potential of +0.25 V in PBS. As shown in Figure 7d, the rGO-PAP-modified electrode shows a remarkable sensing behavior upon the addition of DA (10 μM). There is no significant current response upon adding equimolar chemical species. Especially, the addition of AA and UA does not affect the current density of the rGO-PAP-modified electrode. In addition, the DPV measurement is carried out in 1 μM DA/5-fold concentrations of various potential interferents (Figure S3). These chemical species have no tangible impact on the DA's current response. These results

https://doi.org/10.1021/acsami.1c18137
ACS Appl. Mater. Interfaces 2021, 13, 60878−60893

Table 1. Comparison of Various Electrodes Used for DA Sensing Application[a]

group	modified electrode materials	linear range (μM)	LOD (nM)	ref
metal-based	rGO-Pt	10−170	250	60
	rGO-Pd NPs	1−150	233	61
	rGO-AuNPs/ITO	0.02−200	15	62
	rGO-SS	1−1000	<1000	63
	TiN-rGO	5−175	159	64
metal-free	rGO-PTA	0.5−20		65
	rGO-MWNT-PTA	0.5−20	1.14	66
	3D SWNT-PPy composite	5−50	5000	67
	rGO-GC	0.1−100	100	38
	carbon fiber		41	68
	carbon NRs	1−10	60	69
	POMF-rGO	1−200	80.4	70
	HOPG-β-cyclodextrin		100	71
hybrid/composite	NACP	0.05−15	10.9	15
	MIP/MWCNT/GAs/GCE	0.005−20	1670	72
	SPANI/CNSs/GCE	0.5−1780	15	73
metal-free	rGO-PAP	0.01−100	7.5	this work

[a]NP: nanoparticle, SS: stainless steel, NT: nanotube, NR: nanorod, PTA: phospotungstic acid, PPy: polypropylene, MWCNT: multiwall carbon nanotube, GC: glassy carbon, POMF: polyoxometalate-based metal−organic framework, HOPG: highly oriented pyrolytic graphite, NACP: Ni-MOF composite/AuNPs/CNTs/PDMS, SPANI: sulfonated polyaniline, CNS: carbon nanospheres.

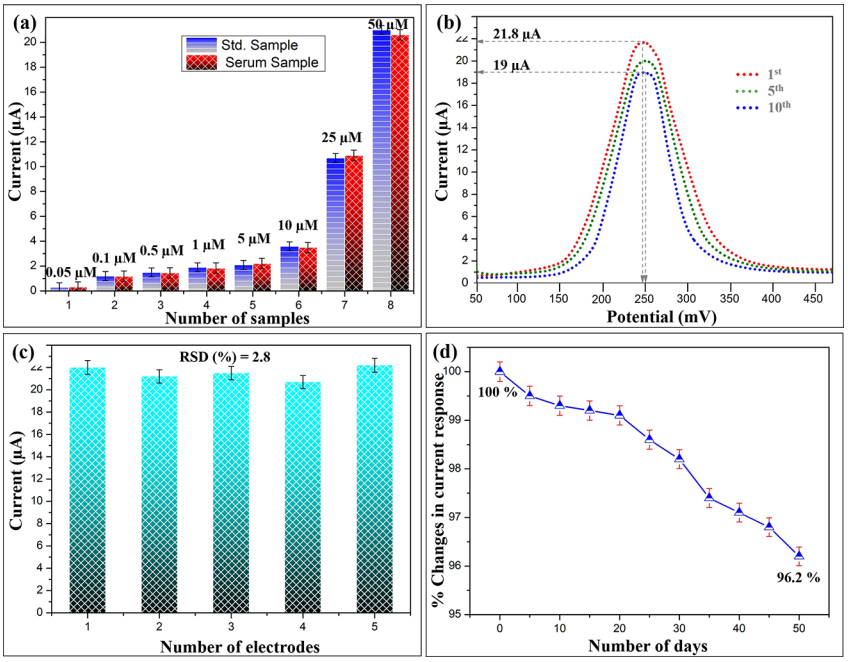

Figure 9. (a) Analysis result of the current response for the standard and serum real samples. Error bar: standard deviation of three samples measurement (n = 3). (b) DPV curves of the rGO-PAP-modified electrode in the PBS containing 50 μM DA, which was recorded for 10 cycles by reusing the same modified electrode materials. (c) Current responses of five parallelly fabricated rGO-PAP-modified electrodes toward 50 μM DA. Error bar: standard deviation of eight samples measurement (n = 8). (d) Chart of change in current against the number of days. Error bar: standard deviation of eight samples measurement (n = 8).

are consistent with the CV and DPV studies and further validate the excellent specificity of the rGO-PAP nanoscale materials for DA detection.

2.3.2. Sensitivity Analysis. To investigate the sensitivity of the rGO-PAP-modified electrode toward DA, the DPV and amperometric experiments were performed in 100 mM PBS solution under different concentrations (0.01−100 μM) along with 20 μM AA and UA. As can be observed in Figure 8a, the current of the anodic peak increases with the concentration of DA at a potential of 0.25 V. The modified electrode exhibits an excellent linear range of detection against the concentration of DA (Figure 8b). The relationship between the current response I_{pa} (in μA) and the concentration of DA C_{DA} (μM) is I_{pa} = 0.41038 C_{DA} + 0.3885. The limit of detection (LOD) for this rGO-PAP sensor is determined to be 7.5 nM (signal/noise = 3).

The amperometric study displays a similar result, where the current response increases significantly upon each addition of DA and exhibits a good linear relationship with the DA concentration as illustrated in Figure 8c. A fast current

https://doi.org/10.1021/acsami.1c18137
ACS Appl. Mater. Interfaces 2021, 13, 60878−60893

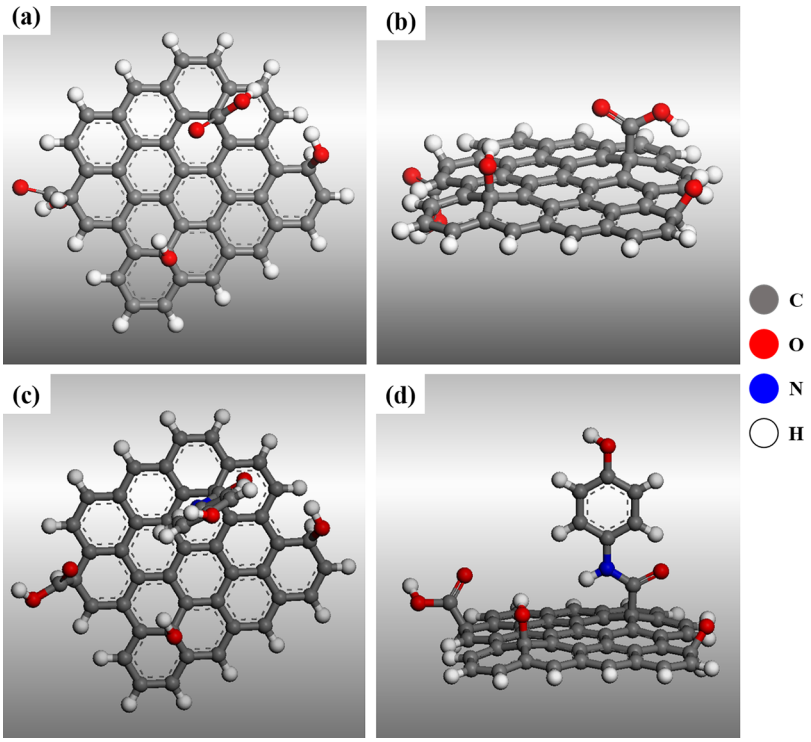

Figure 10. (a/c) Top view of the optimized structures of the pristine rGO/PAP-functionalized rGO. (b/d) Side view of the optimized structures of the pristine rGO/PAP-functionalized rGO. PAP is bonded with rGO via an amide-type bond at the center of the basal plane.

response is observed when 50 μM DA is added into the 100 mM PBS solution. The steady-state current reaches nearly 90% within 3 s. It recovers to 10% of the baseline in less than 2.8 s after fast dilution (Figure 8d). For comparison, the sensing ability of previously reported carbon-based electrodes is presented in Table 1. Obviously, both the linear range and LOD of the rGO-PAP sensor exceed those of others for sensing neurotransmitter DA.

2.3.3. Practicality, Stability, Reproducibility, and Durability Analyses. For examining the commercial applicability of our sensor, fundamental factors such as real-sample, stability, reproducibility, and durability analyses are investigated in this section. The fabricated sensor is subjected to detect DA in a wide range of human serum assays (0.05−050 μM) to evaluate its practical application. Figure 9a illustrates that the current responses for the standard and real samples are similar. They show reasonable recovery ranging from 97 to 105.6% with an acceptable relative standard deviation (RSD) of 1.4−3.3%. The samples (25 and 50 μM spiked) were cross-verified by the high-performance liquid chromatography (HPLC) analysis and are in good agreement with our reported data (Table S6). Hence, this sensor can be used for clinical sample analysis.

In Figure 9b, the peak current signal retains about 98% of the initial value even after 10 cycles, indicating that rGO-PAP is more efficient in sensing DA than the other metal-free biosensors (Table 1). To evaluate the reproducibility, we have parallelly prepared five rGO-PAP-modified electrodes under the same conditions. The similar current response (RSD 2.8%) for all of the electrodes shown in Figure 9c proves a good reproducibility of the fabrication method. Figure 9d shows the durability test chart of the rGO-PAP. The electrochemical performance was evaluated every 5 days for 50 days; 96.2% of the current signal and the working function are retained, which implies that the material is stable for a long time under normal storage conditions.

2.3.4. Fabrication of Flexible-Printed Electronics. Various colloidal rGO-PAP inks are prepared by dispersing the as-synthesized rGO-PAP in water, ethanol, dimethylsulfoxide (DMSO), and isopropyl alcohol (IPA). All colloidal solutions exhibit very good stability (2 months) at a concentration up to 10 mg mL^{-1}, as shown in Figure S8a. The shelf-life stability is analyzed by leaving the colloidal solution uninterrupted for various times. Figure S9a,b shows the UV−vis and dynamic light scattering (DLS) spectra of the colloidal rGO-PAP/ethanol solution at different times, respectively. The absorbance and average size remain almost stable for 30 days. And also, we demonstrate the potential application of well-dispersed rGO-PAP gravure ink in the fabrication of flexible-printed electronics. As presented in Figure S6c,d,e, simple and complex patterns can be fabricated on various flexible substrates such as paper, polyimide, and aluminum foil, respectively.

2.4. Computational Study of Molecular Interactions among rGO, PAP, and DA. The surface modifications and stable molecular structures were calculated using the density functional theory (DFT) to understand the possible reaction mechanism as well as the adsorption model. (Full details of the DFT calculation are given in the Experimental Methods section.) FT-IR, XPS, and EDS analyses have already confirmed that the PAP molecules are linked with rGO via amide-type bonding. We first calculated the energy for the formation of the amide-, ester-, and ether-type bonds at the interfaces between rGO and PAP. $\Delta G_{\text{amide bond}} = -0.436$ kcal mol^{-1} while $\Delta G_{\text{ester bond}} = 5.729$ kcal mol^{-1}, meaning that the formation of the amide bond is more favorable than the ester bond on the rGO surface. Figure S4 displays the feasible formation mechanism of the amide-type bond.

https://doi.org/10.1021/acsami.1c18137
ACS Appl. Mater. Interfaces 2021, 13, 60878−60893

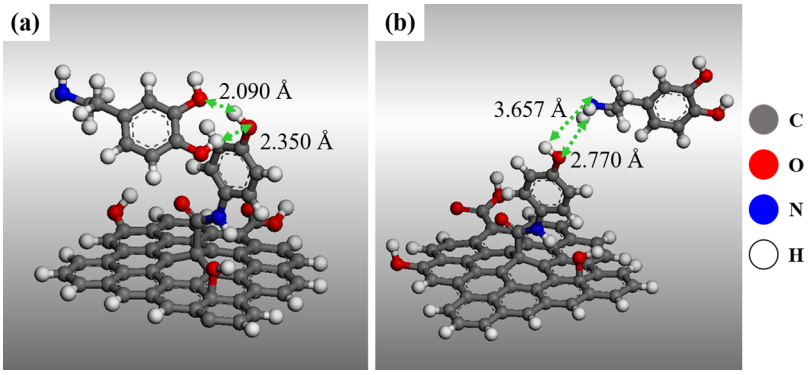

Figure 11. (a/b) Side view of the optimized structures of DA molecule adsorbed on the rGO-PAP via −OH/−NH sites.

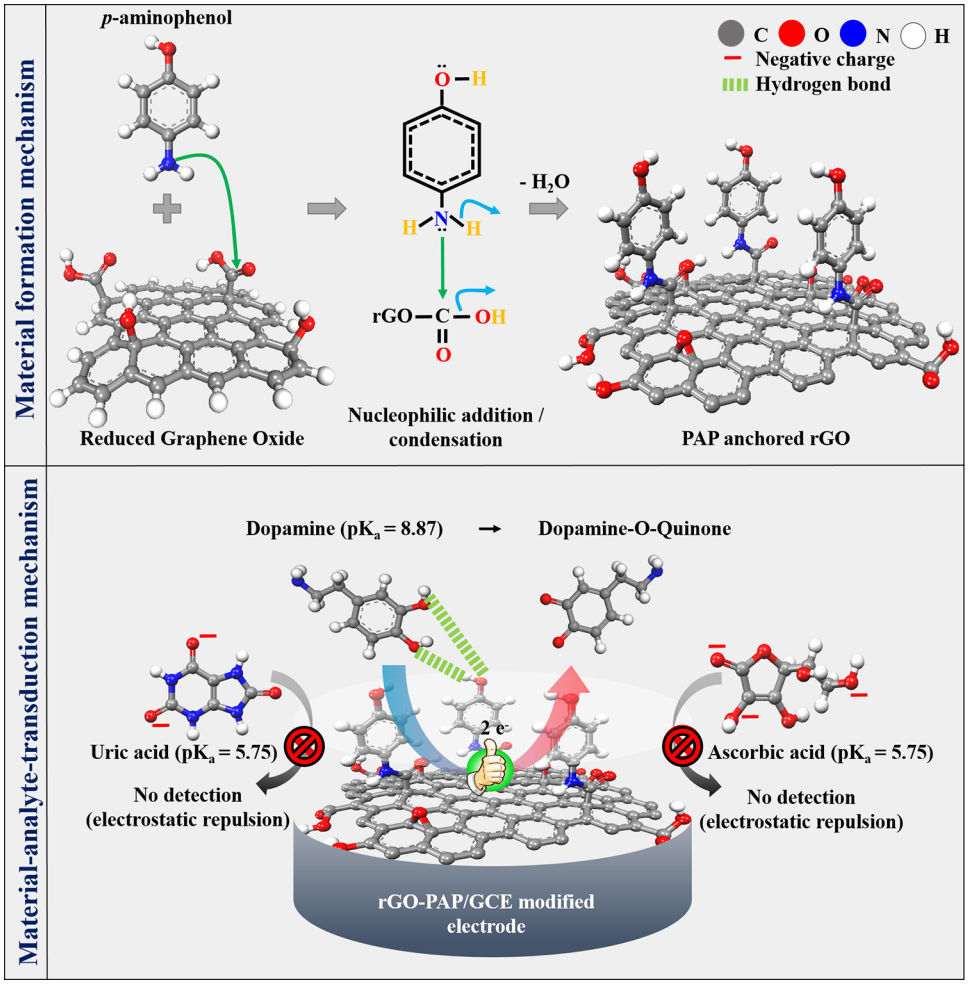

Figure 12. Schematic for the comprehensive mechanism of the material−analyte transduction.

The PAP molecular is possible to be bonded with rGO at either the basal or edge plane. Based on the energy optimization results of constructing the pristine rGO and linking PAP with rGO via an amide bond, we found that the preferred bonding position of PAP is at the basal region of rGO (Figure 10). This bonding position reforms the planar structure of the pristine rGO and results in wrinkled-paper-like morphology as observed in the TEM (Figure 2) and STM (Figure 5) results. Our synthesized material shows a nearly uniform distribution of PAP molecule over the rGO surface as reported in an earlier work of Bueno et al. and Ambrosio et al., where they have shown that the organic molecule with amine functional groups tends to form covalent linkage over the graphene/graphite structure at the basal plane.[74,75]

In this unique functionalized rGO-PAP, the free hydroxyl terminal group acts as an interaction site for the biomolecules. There are two possible ways to adsorb and connect the DA molecule with the rGO-PAP surface, which can be represented as type-1 and type-2 hydrogen (H) bonds as shown in Figure S5. The free energy of forming type-1 H-bond was found to be less than that of type-2, inferring that type-1 is preferred. Figure 11 depicts that the length of the H-bond in the $-NH_2$

https://doi.org/10.1021/acsami.1c18137
ACS Appl. Mater. Interfaces 2021, 13, 60878−60893

site of DA is larger than that in the −OH site. The DA molecule can be adsorbed on rGO-PAP via both amine and hydroxyl groups. However, the distance is too large for an amine site and its adsorption energy is obviously weaker than that of the hydroxyl site, indicating that it is not the preferred configuration. Based on the thermodynamic properties, we can conclude that the possible interaction between DA and rGO-PAP is through hydrogen bonding at the site of −OH.

2.5. Comprehensive Mechanism of Material−Analyte Transduction. As analyzed above, the possible interaction sites between rGO and PAP are −COOH/−OH (in rGO) and $-NH_2$/−OH (in PAP). The rGO structure consists of a few oxide functional groups at their surfaces and edges. Depending on the reaction medium, they are active or inactive. PAP is a reducing agent and tends to be oxidized in an alkaline medium. In an appropriate reaction medium, it can become a strong nucleophile ion. A few reports deal with the amine functionalization of rGO containing both amine and hydroxyl functional groups, which can result in free $-NH_2$ terminal groups or free −OH terminal groups based on the synthetic approach.[52]

In this study, the carboxyl group in rGO tends to lose an −OH ion and form a carbonium (+C═O) ion. Owing to its lower electronegativity than O (−OH), N ($-NH_2$) tends to be bonded with rGO. It attracts the carbonium ion through electrostatic attraction, which is similar to the reported phenomenon in the interaction between *p*-nitrophenol and graphene.[76] These results imply that one can engineer the molecular interaction sites via tuning the reaction medium. Thus, the interaction of these intermediate molecules leads to the formation of amide-type covalent linkage through the carboxyl site of rGO and amine site of PAP (refer to the schematic reaction mechanism shown in Figure S4). The results of XPS, FT-IR, NMR, and EDS confirm these descriptions.

As discussed earlier in the Section 2.3, the sensing of DA entails an oxidation process that generates its counterpart dopamine-*O*-quinone. The two OH groups in DA get dehydrogenated into O atoms during the electrocatalytic reaction, which means that the electron transportation via the interaction site of the molecule can be key to probing the minute changes in the molecule. To gain further insight into the electronic properties of the anchored PAP molecules with rGO, we have calculated the electron density and charge distribution as shown in Figure S7. The analysis of the Mulliken charge population of atoms related to the covalent linkage of rGO-PAP could provide insight into the change of amide bond interaction to the basal plane of rGO. The negative Mulliken charge of the carbon atom can be ordered as C1 > C2 > C3 > C4, which are labeled in the corresponding Figure S7c. This indicates that the Mulliken charge of the C1 atom gets more negative after surface modification than the other functional group site, and also the carbon species belonging to the bridge site of reduced graphene oxide become more negative compared to the same atoms in pristine structure too.

Interestingly, the amide-bond-connected C atom in the proposed structure has an unbalanced charge and shows more negative charge than the other surrounded C atoms in the rGO planes and also the −O atom in PAP has more charge than the other O atom on the rGO sheet. By our novel facile synthetic approach, we have designed the rGO-PAP with a free OH terminal group, which is more favorable for making hydrogen bonds with two OH sites of DA rather than NH_2 tail. Overall, we believe that the intriguing sensitivity and selectivity properties of rGO-PAP can be attributed to the following factors: (i) the rapid charge transfer in rGO-PAP via $\pi-\pi$ electron coupling/resonance effect during the operation as shown in Figure S6 and (ii) the formation of the stable and strong type-1 H-bond between DA and rGO-PAP. The schematic of the comprehensive mechanism of the material−analyte transduction is illustrated in Figure 12.

3. CONCLUSIONS

A novel all-organic-based biosensor has been developed by precisely covalent-linking PAP with rGO. The sensor owns high selectivity and sensitivity for the detection of the neurotransmitter DA. This technique provides a facile synthetic approach to obtain more economical electrode materials in comparison to the available metal-doped (Au, Pt, Pd, etc.) or metal-free high processed materials such as those derived from highly processed graphene, single-wall carbon nanotube (SWCNT), multiwall carbon nanotube (MWCNT), polymer-rGO, metal−organic framework (MOF), and other nanocomposites. The as-synthesized material rGO-PAP is subjected to various analytical techniques to decipher its complete physicochemical characteristics. These results reveal that the nanostructure rGO-PAP possesses crystalline graphene oxide layers with wrinkled-paper-like morphology. A comprehensive mechanism of material−analyte transduction based on our experimental and DFT studies is provided, which sheds more light on the functionalization mechanism as well as the selectivity toward the DA molecule. The electrode rGO-PAP not only enhances the peak current significantly but also decreases the overpotential of DA oxidation and eliminates the interference of AA and UA. The calculated value of the detection limit of this rGO-PAP sensor was found to be 7.5 nM in the presence of potential interferents with a wide linear range, 0.01−100 μM, which is very much lower than that of the recently reported metal-free sensors and metal-based sensors. Also, we demonstrate the potential application of well-dispersed rGO-PAP gravure ink in the fabrication of flexible-printed electronics. Our results prove that one can construct a robust, reasonable, and scalable biosensor for real diagnostic device applications by simply engineering the interface between the rGO surface and a simple organic molecule.

4. EXPERIMENTAL METHODS

4.1. Chemicals. rGO and DA (>99%) were purchased from Sigma-Aldrich. UA, AA, glucose, glutamic acid, epinephrine, serotonin, norepinephrine, sulfuric acid, PAP, methanol, dichloromethane (DCM), potassium hexacyanoferrate(III) ($K_3Fe(CN)_6$), potassium hexacyanoferrate(II) trihydrate ($K_4Fe(CN)_6{\cdot}3H_2O$), potassium chloride (KCl), dimethylsulfoxide (DMSO), and isopropyl alcohol (IPA) were purchased from Merck. Stock solutions of DA (1.0 mM and various concentrations) were prepared by dissolving the required amount of the compounds in Milli-Q water (18.2 MΩ·cm). PBS consisting of KH_2PO_4 and K_2HPO_4 with pH 7.2 was used as a supporting electrolyte. All solvents and reagents used in the present study were of analytical grade and used as received unless otherwise mentioned.

4.2. Preparation of rGO-PAP. rGO (10 mg) was added into a round-bottom flask containing 20 mL of DCM and sonicated for 15 min. Then, 20 mg of PAP was added slowly as five individual batches (each batch containing 4 mg) with constant stirring at temperatures of 5−10 °C. After stirring for 10 min, a few drops (∼3 mL) of sulfuric

https://doi.org/10.1021/acsami.1c18137
ACS Appl. Mater. Interfaces 2021, 13, 60878−60893

acid were added and the mixture was refluxed for 12 h. The final product was cooled, filtered, and washed with DCM (2 × 5 mL) and methanol (3 × 5 mL). Finally, the wet solid was washed with Milli-Q water till all of the washings were neutral, which was monitored by a pH meter. The obtained sample was dried in an oven at 40−45 °C for 2 h and stored in a dry vacuum desiccator for further study.

4.3. Materials Characterization. The crystalline phases of the materials were characterized by XRD using a Rigaku D/max 2200V/PC diffractometer with Cu Ka radiation (λ = 1.54178 Å). A Lab Ram Horiba-Jobin Yvon spectrometer coupled with an Olympus metallographic microscope was used for Raman spectroscopy measurements in a backscattering mode. A diode-pumped solid-state laser with a wavelength of 532.08 nm was used for excitation. A 100× microscope objective was used, which yields a focused spot diameter of ~1 μm. All of the spectra were recorded at an exposition time of 5 s. Before and after the acquisition of each Raman spectrum, the first-order Raman spectrum of monocrystalline silicon was measured as a reference and the spectra were calibrated concerning the silicon peak position at 520 ± 1 cm^{-1}. High-resolution transmission electron microscopy (HRTEM) and EDS analyses were carried out in an FEI Tecnai G2 F30 microscope in which an electron beam is generated from the field emission gun at 300 keV. AFM and STM measurements were carried out in an Oxford instruments-Asylum Research microscope "Cypher S AFM". Measurements were performed in a dynamic mode, using the amplitude as a feedback channel for topographic determination. It can provide information on the thickness of rGO-PAP, layer-dependent distribution of charge, electrical potential, and work function. XPS using a Thermo Electron Corporation ESCA Lab250 spectrometer at 15 kV and 150 W was employed to study the surface characteristic of the synthesized samples. FT-IR spectroscopic analyses were performed using an FTIR spectrometer Vertex 70V (BRUKER GmbH), a KBr disk containing 0.1 mg of synthesized rGO-PAP, as well as pristine rGO were recorded. The average size of the colloidal particles was measured by the dynamic light scattering technique (DLS, Malvern Panalytical Zetasizer Nano ZS). Light absorption (UV−vis spectra) of products was performed by a Shimadzu UV-2401PC instrument. An ultrasound bath cleaner was used for the dispersion of rGO-PAP. Solid-state nuclear magnetic resonance spectroscopy (NMR) experiments were carried out on an Agilent DD2-600 MHz NMR spectrometer.

4.4. Electrochemical Analysis System. All of the electrochemical studies were carried out via an electrochemical workstation (Autolab, PGSTAT302N). A conventional three-electrode system consisting of a modified glassy carbon electrode (GCE) as the working electrode and the platinum auxiliary electrode and silver chloride as reference electrodes were employed in voltammetric detection. All electrochemical measurements were performed using N_2-saturated 0.1 M PBS (pH = 7.2) as the supporting electrolyte at 25 ± 1 °C. The cyclic voltammograms were obtained by scanning the potential from −1.0 to +1.0 V vs Ag/AgCl and at a scan rate of 100 mV s^{-1}.

Differential pulse voltammograms were recorded by scanning the potential from −0.10 to 0.70 V with a pulse height of 100 mV, a pulse time of 0.4 s, a voltage step time of 0.5 s, and a voltage step height of 1 mV. The DPV curves were plotted after baseline correction using a spline fit by selecting points along the curve both preceding and proceeding the potential range corresponding to the faradaic peak and interpolating the fitted curve through these points, which is done by OriginPro software.

The amperometric study was carried out at +0.25 V by successively adding DA in PBS along with an equal molar concentration of potential interferents including glucose, glutamic acid, potassium ions (K^+), chloride ions (Cl^-), AA, and UA under constant stirring.

For real-sample analysis, human blood serum was used to evaluate the performance of the rGO-PAP electrode toward DA. The sample was prepared as follows: 100 μL of serum was diluted in 25 mL of 0.1 M PBS solution. Then, the diluted serum was spiked with a known amount of DA; five different concentrations were tested (0.05, 0.1, 0.5, 1, 5, 10, 25, and 50 μM). The recoveries and RSD of DA concentrations were determined by measuring the current at 0.25 V relative to the reference electrode.

The surface of the working electrode was polished with an aqueous slurry of alumina nanopowder (LabChem) using SiC-emery paper (with various sizes 1 and 0.05 μm). rGO-PAP (1.5 mg) was dispersed in 1 mL of Milli-Q water and 0.4 mL of ethanol solution. This prepared solution was sonicated for 10 min. Finally, 5 μL of this rGO-PAP solution was transferred to the surface of a precleaned working electrode (GCE). It was dried at room temperature and finally employed for further electrochemical analysis.

First, a calibration curve is determined by plotting a current response vs the known amount of dopamine (DA) in a standard solution. The number of samples used for the test is eight and plotted with a standard deviation error bar. Later, various DA spiked serum samples are introduced to the three-electrode electrochemical system container and the DPV measurement is performed. The current response of each sample is recorded and fitted to the calibration curve, which provides a corresponding concentration.

4.5. Computational Methods. All of the calculations including geometrical characteristics, energetics and thermodynamics, and electron density properties of model structures were conducted by density functional calculations using DMol3 code of Materials Studio modeling and simulation software. The geometrical structures were optimized without imposing any symmetry. Calculations have been performed using the gradient-corrected (GGA) BLYP exchange−correlation functional. The atomic orbital basis set was assigned as double numerical plus polarization (DNP) and the self-consistent field (SCF) tolerance set to 10^{-6}. The model of rGO discussed here contains 42 carbon, 17 hydrogen atoms, 2 −COOH, and 2 −OH groups both on edge and basal planes. All of the products and reactant molecules underwent a refinement process known as optimization, in which the coordinates of the atoms are adjusted to bring the energy of the structure to a stationary point. The thermodynamic parameters enthalpy (H), entropy (S), free energy (G), and heat capacity were calculated at constant pressure (C_p) under different chemical reaction temperatures. The reaction H or G of the corresponding chemical reactions shown in Figure S4 was determined from the first-principle calculations. The results were obtained from a geometry optimization using DMol3, which provides the information of the total energy (electronic and ionic) (E_{tot}) and Gibbs free energy ($G_{tot}^{298.15K}$) of the system at 298.15 K.

The total correlated energy is given by

$$E_{totCorr}^{298.15k} = E_{tot} + G_{tot}^{298.15k}$$

And the Gibbs free energy of the reaction is given by:

$$\Delta G_{Reaction} = E_{totCorr}^{298.15k}\,(\text{Product}) - E_{totCorr}^{298.15k}\,(\text{Reactant})$$

The interaction of the DA molecule with the rGO-PAP structure via H-bond as shown in Figure S5 is calculated as: $E = E_{rGO\text{-}PAP\text{-}DA} - (E_{rGO\text{-}PAP} + E_{DA})$. The contribution to the atomic charge from each atomic orbital was calculated by population analysis, which is assigned as the Mulliken atomic orbital/charge.

■ ASSOCIATED CONTENT

Supporting Information

The Supporting Information is available free of charge at https://pubs.acs.org/doi/10.1021/acsami.1c18137.

NMR spectra of as-synthesized rGO-PAP, possible mechanism of DA interacted with the modified rGO-PAP electrode via H-bond, UV/DLS shelf-life stability study of rGO-PAP/ethanol colloidal solution (Figures S1−S9), key factors for designing efficient carbon-based neurotransmitters sensors, Raman spectra peak intensity values of D, G and 2D bands, and moiety fraction data obtained from XPS analysis (Tables S1−S6) (PDF)

https://doi.org/10.1021/acsami.1c18137
ACS Appl. Mater. Interfaces 2021, 13, 60878−60893

AUTHOR INFORMATION

Corresponding Authors

Lijun Wu − *Guangdong Provincial Key Laboratory of Nanophotonic Functional Materials and Devices, School of Information and Optoelectronic Science and Engineering, South China Normal University, Guangzhou 510006, China*; Phone: +86-020-39310366; Email: ljwu@scnu.edu.cn

Neeraj Gupta − *Department of Chemistry and Chemical Sciences, Central University of Himachal Pradesh, Kangra, Himachal Pradesh 176215, India*; orcid.org/0000-0003-0493-5412; Phone: +91-1792-308000; Email: gupta_nrj@hpcu.ac.in

Authors

Jagadeesh Suriyaprakash − *Guangdong Provincial Key Laboratory of Nanophotonic Functional Materials and Devices, School of Information and Optoelectronic Science and Engineering, South China Normal University, Guangzhou 510006, China*; orcid.org/0000-0001-7269-2841

Kanchan Bala − *Department of Chemistry, Sri Guru Granth Sahib World University, Fatehgarh Sahib, Punjab 140407, India*

Lianwei Shan − *School of Materials Science and Engineering, Harbin University of Science and Technology, Harbin 150040, China*; orcid.org/0000-0001-6989-280X

Complete contact information is available at: https://pubs.acs.org/10.1021/acsami.1c18137

Author Contributions

J.S. wrote an original draft and executed the whole project. L.W. and N.G. jointly supervised the project. They were involved at all stages of work including material design, characterization, and explaining the mechanism. LianWei Shan helped with the experiments and interpret the data. Kanchan Bala assisted with the experimental part, especially the electrochemistry experiments.

Notes

The authors declare no competing financial interest.

ACKNOWLEDGMENTS

This work was funded by the National Natural Science Foundation of China (NSFC) (grant nos. 61675070 and 11704133) and Science and Technology Program of Guangzhou (no. 2019050001). J.S. acknowledges CPSF and SCNUPost-Doctoral Fellowship. Project funded by China Postdoctoral Science Foundation (2020M672669). L.S. acknowledges Postdoctoral Scientific Developmental Fund of Heilongjiang Province (LBH-Q16122). J.S. is thankful to Ting Ting Qiao for her professional and personal advice to make this paper into the final shape and help to analyze HPLC data. J.S. is grateful to Dr. Y. T. Zhou, IMR-CAS, for microscopic analysis and fruitful discussion.

REFERENCES

(1) Brinkworth, R. I.; Lloyd, E. J.; Andrews, P. R. Brain Chemistry and Central Nervous System Drugs. *Nat. Prod. Rep.* **1988**, *5*, 363.

(2) Chen, C. H.; Luo, S. C. Tuning Surface Charge and Morphology for the Efficient Detection of Dopamine Under the Interferences of Uric Acid, Ascorbic Acid, and Protein Adsorption. *ACS Appl. Mater. Interfaces* **2015**, *7*, 21931.

(3) Huang, C.; Chen, X.; Lu, Y.; Yang, H.; Yang, W. Electrogenerated Chemiluminescence Behavior of Peptide Nanovesicle and Its Application in Sensing Dopamine. *Biosens. Bioelectron.* **2015**, *63*, 478.

(4) Kruss, S.; Landry, M. P.; Ende, E. V.; Lima, B. M. A.; Reuel, N. F.; Zhang, J.; Nelson, J.; Mu, B.; Hilmer, A.; Strano, M. Neurotransmitter Detection Using Corona Phase Molecular Recognition on Fluorescent Single-Walled Carbon Nanotube Sensors. *J. Am. Chem. Soc.* **2014**, *136*, 713.

(5) Nakatsuka, N.; Abendroth, J. M.; Yang, K.; Andrews, A. M. Divalent Cation Dependence Enhances Dopamine Aptamer Biosensing. *ACS Appl. Mater. Interfaces* **2021**, *13*, 9425.

(6) Yan, Y.; Liu, Q.; Du, X.; Qian, J.; Mao, H.; Wang, K. Visible Light Photoelectrochemical Sensor for Ultrasensitive Determination of Dopamine Based on Synergistic Effect of Graphene Quantum Dots and TiO2 Nanoparticles. *Anal. Chim. Acta* **2015**, *853*, 258.

(7) Saraji, M.; Shahvar, A. Selective Micro Solid-Phase Extraction of Epinephrine, Norepinephrine and Dopamine from Human Urine and Plasma Using Aminophenyl Boronic Acid Covalently Immobilized on Magnetic Nanoparticles Followed by High-Performance Liquid Chromatography-Fluorescence Detection. *Anal. Methods* **2016**, *8*, 830.

(8) Qing, X.; Wang, Y.; Zhang, Y.; Ding, X.; Zhong, W.; Wang, D.; Wang, W.; Liu, Q.; Liu, K.; Li, M.; Lu, Z. Wearable Fiber-Based Organic Electrochemical Transistors as a Platform for Highly Sensitive Dopamine Monitoring. *ACS Appl. Mater. Interfaces* **2019**, *11*, 13105.

(9) Moody, A. S.; Payne, T. D.; Barth, B. A.; Sharma, B. Surface-Enhanced Spatially-Offset Raman Spectroscopy (Sesors) for Detection of Neurochemicals Through the Skull at Physiologically Relevant Concentrations. *Analyst* **2020**, *145*, 1885.

(10) Feng, J.; Guo, H.; Li, Y.; Wang, Y.; Chen, W.; Wang, A. Single Molecular Functionalized Gold Nanoparticles for Hydrogen-Bonding Recognition and Colorimetric Detection of Dopamine with High Sensitivity and Selectivity. *ACS Appl. Mater. Interfaces* **2013**, *5*, 1226.

(11) Xu, C.; Wu, F.; Yu, P.; Mao, L. In Vivo Electrochemical Sensors for Neurochemicals: Recent Update. *ACS Sens.* **2019**, *4*, 3102.

(12) Hernández-Rodríguez, J. F.; Rojas, D.; Escarpa, A. Electrochemical Sensing Directions for Next-Generation Healthcare: Trends, Challenges, and Frontiers. *Anal. Chem.* **2021**, *93*, 167.

(13) Barlow, S. T.; Louie, M.; Hao, R.; Defnet, P. A.; Zhang, B. Electrodeposited Gold on Carbon-Fiber Microelectrodes for Enhancing Amperometric Detection of Dopamine Release from Pheochromocytoma Cells. *Anal. Chem.* **2018**, *90*, 10049.

(14) Yang, Z.; Liu, X.; Zheng, X.; Zheng, J. Synthesis of Au@Pt Nanoflowers Supported on Graphene Oxide for Enhanced Electrochemical Sensing of Dopamine. *J. Electroanal. Chem.* **2018**, *817*, 48.

(15) Shu, Y.; Lu, Q.; Yuan, F.; Tao, Q.; Jin, D.; Yao, H.; Xu, Q.; Hu, X. Stretchable Electrochemical Biosensing Platform Based on Ni-MOF Composite/Au Nanoparticle-Coated Carbon Nanotubes for Real-Time Monitoring of Dopamine Released from Living Cells. *ACS Appl. Mater. Interfaces* **2020**, *12*, 49480.

(16) Jiao, J.; Zuo, J.; Pang, H.; Tan, L.; Chen, T.; Ma, H. A Dopamine Electrochemical Sensor Based on Pd-Pt Alloy Nanoparticles Decorated Polyoxometalate and Multiwalled Carbon Nanotubes. *J. Electroanal. Chem.* **2018**, *827*, 103.

(17) Ivanova, M. N.; Grayfer, E. D.; Plotnikova, E. E.; Kibis, L. S.; Darabdhara, G.; Boruah, P. K.; Das, M. R.; Fedorov, V. E. Pt-Decorated Boron Nitride Nanosheets as Artificial Nanozyme for Detection of Dopamine. *ACS Appl. Mater. Interfaces* **2019**, *11*, 22102.

(18) Bala, K.; Suriyaprakash, J.; Singh, P.; Chauhan, K.; Villae, A.; Gupta, N. Copper and Cobalt Nanoparticles Embedded in Naturally Derived Graphite Electrodes for the Sensing of the Neurotransmitter Epinephrine. *New J. Chem.* **2018**, *42*, 6604.

(19) Pandikumar, A.; How, G. T. S.; See, T. P.; Omar, F. S.; Jayabal, S.; Kamali, K. Z.; Yusoff, N.; Jamil, A.; Ramaraj, R.; John, S. A.; Lim, H. N.; Huang, N. M. Graphene and Its Nanocomposite Material Based Electrochemical Sensor Platform for Dopamine. *RSC Adv.* **2014**, *4*, 63296.

(20) Park, S. J.; Lee, S. H.; Yang, H.; Park, C. S.; Lee, C.; Kwon, O. S.; Park, T. H.; Jang, J. Human Dopamine Receptor-Conjugated

Multidimensional Conducting Polymer Nanofiber Membrane for Dopamine Detection. *ACS Appl. Mater. Interfaces* **2016**, *8*, 28897.
(21) Jiang, L.; Nelson, G. W.; Abda, J.; Foord, J. S. Novel Modifications to Carbon-Based Electrodes to Improve the Electrochemical Detection of Dopamine. *ACS Appl. Mater. Interfaces* **2016**, *8*, 28338.
(22) Fazio, E.; Spadaro, S.; Bonsignore, M.; Lavanya, N.; Sekar, C.; Leonardi, S. G.; Neri, G.; Neri, F. Molybdenum Oxide Nanoparticles for the Sensitive and Selective Detection of Dopamine. *J. Electroanal. Chem.* **2018**, *814*, 91.
(23) Moghzi, F.; Soleimannejad, J.; Sañudo, E. C.; Janczak, J. Dopamine Sensing Based on Ultrathin Fluorescent Metal-Organic Nanosheets. *ACS Appl. Mater. Interfaces* **2020**, *12*, 44499.
(24) Li, J.; Yu, J.; Sun, Z.; Liu, H.; Wang, X. Innovative Integration of Phase-Change Microcapsules with Metal-Organic Frameworks into an Intelligent Biosensing System for Enhancing Dopamine Detection. *ACS Appl. Mater. Interfaces* **2021**, *13*, 41753.
(25) Ba, V. A. P.; Cho, D.; Hong, S. Nafion-Radical Hybrid Films on Carbon Nanotube Transistors for Monitoring Antipsychotic Drug Effects on Stimulated Dopamine Release. *ACS Appl. Mater. Interfaces* **2019**, *11*, 9716.
(26) Meng, L.; Turner, A. F.; Mak, W. C. Modulating Electrode Kinetics for Discrimination of Dopamine by a PEDOT:COOH Interface Doped With Negatively Charged Tricarboxylate. *ACS Appl. Mater. Interfaces* **2019**, *11*, 34497.
(27) Kokulnathan, T.; Ahmed, F.; Chen, S.; Chen, T.; Hasan, P. Z.; Bilgrami, A. L.; Darwesh, R. Rational Confinement of Yttrium Vanadate within Three-Dimensional Graphene Aerogel: Electrochemical Analysis of Monoamine Neurotransmitter (Dopamine). *ACS Appl. Mater. Interfaces* **2021**, *13*, 10987.
(28) Meng, Z.; Stolz, R. M.; Mendecki, L.; Mirica, K. A. Electrically-Transduced Chemical Sensors Based on Two Dimensional Nanomaterials. *Chem. Rev.* **2019**, *119*, 478.
(29) Cao, Q.; Puthongkham, P.; Venton, B. J. Review: New Insights into Optimizing Chemical and 3D Surface Structures of Carbon Electrodes for Neurotransmitter Detection. *Anal. Methods* **2019**, *11*, 247.
(30) Liu, S.; Xing, X.; Yu, J.; Lian, W.; Li, J.; Cui, M.; Huang, J. A Novel Label-Free Electrochemical Aptasensor Based on Graphene-Polyaniline Composite Film for Dopamine Determination. *Biosens. Bioelectron.* **2012**, *36*, 186.
(31) Yang, L.; Liu, D.; Huang, J.; You, T. Simultaneous Determination of Dopamine, Ascorbic Acid And Uric Acid at Electrochemically Reduced Graphene Oxide Modified Electrode. *Sens. Actuators, B* **2014**, *193*, 166.
(32) Butler, D.; Moore, D.; Glavin, N. R.; Robinson, J. A.; Ebrahimi, A. Facile Post-Deposition Annealing of Graphene Ink Enables Ultrasensitive Electrochemical Detection of Dopamine. *ACS Appl. Mater. Interfaces* **2021**, *13*, 11185.
(33) Wu, T.; Alharbi, A.; Kiani, R.; Shahrjerdi, D. Quantitative Principles for Precise Engineering of Sensitivity in Graphene Electrochemical Sensors. *Adv. Mater.* **2018**, *31*, No. 1805752.
(34) Velický, M.; Toth, P. S.; Woods, C. R.; Novoselov, K. S.; Dryfe, R. A. W. Electrochemistry of the Basal Plane Versus Edge Plane of Graphite Revisited. *J. Phys. Chem. C.* **2019**, *123*, 11677.
(35) Zhang, G.; Kirkman, P. M.; Patel, A. N.; Cuharuc, A. S.; McKelvey, K.; Unwin, P. R. Molecular Functionalization of Graphite Surfaces: Basal Plane Versus Step Edge Electrochemical Activity. *J. Am. Chem. Soc.* **2014**, *136*, 11444.
(36) Brownson, D. A.; Banks, C. E. *The Handbook of Graphene Electrochemistry*; Springer-Verlag London Ltd, 2014; ISBN 978-1-4471-6427-2.
(37) Hallfors, N.; Junaibi, S. A.; Liao, K.; Ismail, M.; Isakovic, A. Reduced Graphene Oxide for the Design of Electrocardiogram Sensors: Current Status And Perspectives. In *The Iot Physical Layer*; Springer, 2019; p 3.
(38) Wang, H.; Ren, F.; Wang, C.; Yang, B.; Bin, D.; Zhang, K.; Du, Y. Simultaneous Determination of Dopamine, Uric Acid and Ascorbic Acid Using a Glassy Carbon Electrode Modified with Reduced Graphene Oxide. *RSC Adv.* **2014**, *4*, 26895.
(39) Berke, J. D. What Does Dopamine Mean? *Nat. Neurosci.* **2018**, *21*, 787.
(40) Wise, R. A. Dopamine, Learning and Motivation. *Nat. Rev. Neurosci.* **2004**, *5*, 483.
(41) Papalini, S.; Beckers, T.; Vervliet, B. Dopamine: from Prediction Error to Psychotherapy. *Transl. Psychiatry* **2020**, *10*, No. 164.
(42) Perez de la Mora, M.; Hernandez-Mondragon, C.; Crespo-Ramirez, M.; Rejon-Orantes, J.; Borroto-Escuela, D. O.; Fuxe, K. Conventional and Novel Pharmacological Approaches to Treat Dopamine-Related Disorders: Focus on Parkinson's Disease and Schizophrenia. *Neuroscience* **2019**, *439*, 309.
(43) Beaulieu, J. M.; Gainetdinov, R. R. Signaling and Pharmacology of Dopamine Receptors. *Pharmacol. Rev.* **2011**, *63*, 182.
(44) Wang, G. J.; Volkow, N. D.; Logan, J.; Pappas, N. R.; Wong, C. T.; Zhu, W.; Netusll, N.; Fowler, J. S. Brain Dopamine and Obesity. *Lancet* **2001**, *357*, 354.
(45) Michaelides, M.; Thanos, P. K.; Volkow, N. D.; Wang, G. J. Dopamine-Related Frontostriatal Abnormalities in Obesity and Binge-Eating Disorder: Emerging Evidence for Developmental Psychopathology. *Int. Rev. Psychiatry* **2012**, *24*, 211.
(46) Kudin, K. N.; Prud'homme, R. K.; Ozbas, B.; Aksay, I. A.; Schniepp, H. C.; Car, R. Raman Spectra of Graphite Oxide and Functionalized Graphene Sheets. *Nano Lett.* **2008**, *8*, 36.
(47) Bruna, M.; Ott, A. K.; Ijäs, M.; Yoon, D.; Sassi, U.; Ferrari, A. C. Doping Dependence of the Raman Spectrum of Defected Graphene. *ACS Nano* **2014**, *8*, 7432.
(48) Nourbakhsh, A.; Cantoro, M.; Li, B.; Müller, R.; De Feyter, S.; Heyns, M. M.; Sels, B. F.; Gendt, S. D. Tunable N- and P-Type Doping of Single-Layer Graphene by Engineering its Interaction with the SiO_2 Support. *Phys. Status Solidi RRL* **2012**, *6*, 53.
(49) Joshi, N.; Silva, L.; Jadhav, H.; Shimizu, F.; Suman, P.; M'Peko, J.; Orlandi, M.; Seo, J.; Mastelaro, V.; Oliveir, O., Jr. Yolk-Shelled ZnCo2O4 Microspheres: Surface Properties and Gas Sensing Application. *Sens. Actuators, B* **2018**, *257*, 906.
(50) Mishra, R.; Choi, G.; Sohn, Y.; Lee, S.; Gwag, J. A Novel RGO/N-RGO Supercapacitor Architecture for a Wide Voltage Window, High Energy Density and Long-Life Via Voltage Holding Tests. *Chem. Commun.* **2020**, *56*, 2893.
(51) Wang, R.; Lin, Y.; Chen, P.; Chen, H.; Chiu, W. Anomalous Output Performance Enhancement of RGO-Based Triboelectric Nanogenerators by Cu-Bonding. *Nano Energy* **2021**, *86*, No. 106126.
(52) Augustine, S.; Kumar, P.; Malhotra, B. D. Amine-Functionalized MoO3@RGO Nanohybrid-Based Biosensor for Breast Cancer Detection. *ACS Appl. Bio Mater.* **2019**, *2*, 5366.
(53) Greenwood, J.; Phan, T. H.; Fujita, Y.; Li, Z.; Ivasenko, O.; Vanderlinden, W.; Gorp, H. V.; Frederickx, W.; Lu, G.; Tahara, K.; Tobe, Y.; Uji-i, H.; Mertens, S. F. L.; Feyter, S. D. Covalent Modification of Graphene and Graphite Using Diazonium Chemistry: Tunable Grafting and Nano-Manipulation. *ACS Nano* **2015**, *9*, 5520.
(54) Xia, Z.; Kovtun, A.; Leonardi, F.; Li, R.; Gobbi, M.; Feng, X.; Liu, Y.; Bellani, V.; Orgiu, E.; Samorì, P.; Liscio, A.; Treossi, E.; Palermo, V. Electrochemical Functionalization of Graphene at the Nanoscale with Self-Assembling Diazonium Salts. *ACS Nano* **2016**, *10*, 7125.
(55) Puthongkham, P.; Venton, B. J. Nanodiamond Coating Improves the Sensitivity and Antifouling Properties of Carbon Fiber Microelectrodes. *ACS Sens.* **2019**, *4*, 2403.
(56) Elgrishi, N.; Rountree, K. J.; McCarthy, B. D.; Rountree, E. S.; Eisenhart, T. T.; Dempsey, J. L. A Practical Beginner's Guide to Cyclic Voltammetry. *J. Chem. Educ.* **2018**, *95*, 197.
(57) Laviron, E. General Expression of the Linear Potential Sweep Voltammogram in the Case of Diffusionless Electrochemical Systems. *J. Electroanal. Chem. Interfacial Electrochem.* **1979**, *101*, 19.
(58) Huang, Q.; Zhang, H.; Hu, S.; Li, F.; Weng, W.; Chen, J.; Wang, Q.; He, Y.; Zhang, W.; Bao, X. A Sensitive and Reliable

Dopamine Biosensor was Developed Based on the Au@Carbon Dots−Chitosan Composite Film. *Biosens. Bioelectron.* **2014**, *52*, 277.
(59) Huang, Q.; Lin, X. F.; Tong, L.; Tong, Q. X. Graphene Quantum Dots/Multiwalled Carbon Nanotubes Composite-Based Electrochemical Sensor for Detecting Dopamine Release from Living Cells. *ACS Sustainable Chem. Eng.* **2020**, *8*, 1644.
(60) Xu, T.; Zhang, Q.; Zheng, J.; Lv, Z.; Wei, J.; Wang, A.; Feng, J. Simultaneous Determination of Dopamine and Uric Acid in the Presence of Ascorbic Acid Using Pt Nanoparticles Supported on Reduced Graphene Oxide. *Electrochim. Acta* **2014**, *115*, 109.
(61) Palanisamy, S.; Ku, S.; Chen, S. Dopamine Sensor Based on a Glassy Carbon Electrode Modified with a Reduced Graphene Oxide and Palladium Nanoparticles Composite. *Microchim. Acta* **2013**, *180*, 1037.
(62) Huang, X.; Shi, W.; Bao, N.; Yu, C.; Gu, H. Electrochemically Reduced Graphene Oxide and Gold Nanoparticles on an Indium Tin Oxide Electrode for Voltammetric Sensing Of Dopamine. *Microchim. Acta* **2019**, *186*, No. 310.
(63) Farajikhah, S.; Innis, P.; Paull, B.; Wallace, G.; Harris, A. Facile Development of a Fiber-Based Electrode for Highly Selective and Sensitive Detection of Dopamine. *ACS Sens.* **2019**, *4*, 2599.
(64) Feng, J.; Li, Q.; Cai, J.; Yang, T.; Chen, J.; Hou, X. Electrochemical Detection Mechanism of Dopamine and Uric Acid on Titanium Nitride-Reduced Graphene Oxide Composite with and without Ascorbic Acid. *Sens. Actuators, B* **2019**, *298*, No. 126872.
(65) Zhang, H.; Xie, A.; Shen, Y.; Qiu, L.; Tian, X. Layer-By-Layer Inkjet Printing of Fabricating Reduced Graphene-Polyoxometalate Composite Film For Chemical Sensors. *Phys. Chem. Chem. Phys.* **2012**, *14*, 12757.
(66) Ling, Y.; Huang, Q.; Zhu, M.; Feng, D.; Li, X.; Wei, Y. A Facile One-Step Electrochemical Fabrication af Reduced Graphene Oxide−Mutilwall Carbon Nanotubes−Phospotungstic Acid Composite for Dopamine Sensing. *J. Electroanal. Chem.* **2013**, *693*, 9−15.
(67) Min, K.; Yoo, Y. Amperometric Detection of Dopamine Based on Tyrosinase-SWNTS-PPY Composite Electrode. *Talanta* **2009**, *80*, 1007.
(68) Demuru, S.; Deligianni, H. Nafion Coatings for Enhanced Dopamine, Serotonin and Adenosine Sensing. *J. Electrochem. Soc.* **2017**, *164*, G129.
(69) Demuru, S.; Nela, L.; Marchack, N.; Holmes, S.; Farmer, D.; Tulevski, G.; Lin, Q.; Deligianni, H. Scalable Nanostructured Carbon Electrode Arrays for Enhanced Dopamine Detection. *ACS Sens.* **2018**, *3*, 799.
(70) Zhang, W.; Jia, G.; Li, Z.; Yuan, C.; Bai, Y.; Fu, D. Selective Electrochemical Detection of Dopamine on Polyoxometalate-Based Metal-Organic Framework and Its Composite with Reduced Graphene Oxide. *Adv. Mater. Interfaces* **2017**, *4*, No. 1601241.
(71) Li, Z.; Guyse, J.; Rosa, V.; Gorp, H.; Walke, P.; Rodríguez González, M.; Uji-i, H.; Hoogenboom, R.; Feyter, S.; Mertens, S. One-Step Covalent Immobilization of β-Cyclodextrin on Sp2 Carbon Surfaces for Selective Trace Amount Probing of Guests. *Adv. Funct. Mater.* **2019**, *29*, No. 1901488.
(72) Ma, X.; Gao, F.; Dai, R.; Liu, G.; Zhang, Y.; Lu, L.; Yu, Y. Novel. Electrochemical Sensing Platform Based on a Molecularly Imprinted Polymer-Decorated 3D-Multi-Walled Carbon Nanotube Intercalated Graphene Aerogel for Selective and Sensitive Detection of Dopamine. *Anal. Methods* **2020**, *12*, 1845.
(73) Fu, Y.; Sheng, Q.; Zheng, J. The Novel Sulfonated Polyaniline Decorated Carbon Nanosphere Nanocomposites for Electrochemical Sensing of Dopamine. *New J. Chem.* **2017**, *41*, 15439.
(74) Bueno, R. A.; Martinez, J. I.; Luccas, R. F.; del Arbol, N. R.; Munuera, C.; Palomares, F. J.; Lopez, M. F.; Lauwaet, K.; Mompean, F.; Thakur, S.; Hernandez, M. G.; Baranowski, J. M.; Martin-Gago, J. A.; Palacio, I.; Strupinski, W. Highly Selective Covalent Organic Functionalization of Epitaxial Graphene. *Nat. Commun.* **2017**, *8*, No. 15306.
(75) Ambrosio, G.; Drera, G.; DiSanto, G.; Petaccia, L.; Daukiya, L.; Brown, A.; Hirsch, B.; Feyter, S. D.; Sangaletti, L.; Pagliara, S. Interface Chemistry of Graphene/Cu Grafted By 3,4,5-Trimethoxyphenyl. *Sci. Rep.* **2020**, *10*, No. 4114.
(76) Kong, X. K.; Sun, Z. Y.; Chen, M.; Chen, C.; Chen, Q. W. Metal-Free Catalytic Reduction of 4-Nitrophenol to 4-Aminophenol by N-Doped Graphene. *Energy Environ. Sci.* **2013**, *6*, 3260.

https://doi.org/10.1021/acsami.1c18137
ACS Appl. Mater. Interfaces 2021, 13, 60878−60893